Research Square

Preprints are preliminary reports that have not undergone peer review.
They should not be considered conclusive, used to inform clinical practice,
or referenced by the media as validated information.

Economic development intensifies flood exposure through migration reversal

Haiqing yang

yanghaiqing@cqu.edu.cn

Chongqing university https://orcid.org/0000-0003-4497-044X

Anhua Ju

Chongqing university

Xingyue Li

Chongqing university

Zhonghua Jiang

Chongqing university

Lixin Peng

Chongqing University

Physical Sciences - Article

Keywords:

Posted Date: June 19th, 2026

DOI: https://doi.org/10.21203/rs.3.rs-9979524/v1

License: This work is licensed under a Creative Commons Attribution 4.0 International License.
Read Full License

Additional Declarations: There is **NO** Competing Interest.

Economic development intensifies flood exposure through migration reversal

Anhua Ju[1], Xingyue Li[1], Haiqing Yang[1*], Zhonghua Jiang[1], Lixin Peng[1]

Author affiliations

[1] State Key Laboratory of Safety and Resilience of Civil Engineering in Mountain Area, School of Civil Engineering, Chongqing University, Chongqing 400045, China.

Corresponding authors: Haiqing Yang (yanghaiqing@cqu.edu.cn)

Floods are among the most disruptive natural hazards, but their consequences depend not only on extreme water events, but also on where people live and how societies manage risk[1–3]. Recent studies show that flood exposure is increasing as settlements expand into flood-prone areas, while the burden remains unevenly distributed across poorer and more socially vulnerable populations[4–6]. Migration is often viewed as a response to environmental stress, yet human movement is also shaped by economic opportunity, social context and adaptive capacity[7–9]. Here we show that vulnerable river basins are not characterized simply by sustained demographic retreat. Instead, many basins shift from early net outmigration to later net in-migration, revealing a reversal in demographic response under persistent flood pressure. This reversal is most pronounced where economic growth strengthens local attraction and protection, enabling people to return to, or remain concentrated within, hazardous basins. These findings extend flood-risk research beyond identifying where exposure accumulates by showing how migration reversal can allow development to reproduce exposure. They suggest that flood protection should be coordinated with land-use governance and settlement planning, so that adaptation does not inadvertently encourage renewed concentration in hazardous places[3,10].

Flooding is one of the most widespread and destructive natural hazards worldwide and continues to impose substantial pressure on human settlements, infrastructure, and regional development[2,11–13]. In riverine and coastal systems, flood risk has continued to intensify under the combined effects of climate change, urban expansion, land-use transformation, and the sustained concentration of population and assets in exposed areas[14,15]. Recent global assessments have shown that flood exposure has continued to increase not only in absolute magnitude, but also in its social unevenness, with low-income and institutionally constrained regions bearing risks disproportionate to their level of development[5,6,14–16]. This uneven pattern is particularly important because flood impacts are determined not only by hazard intensity, but also by the combined effects of exposure, vulnerability, and adaptive capacity. As a result, similar levels of hazard often correspond to markedly different demographic and socioeconomic consequences under different development contexts[17–19]. Studies based on satellite remote sensing and high-resolution settlement data have shown that the global population exposed to flooding increased significantly during 2000–2015, and that settlement expansion in high-risk flood zones has remained rapid since the mid-1980s[1,3]. Floodplain settlement patterns vary with flood-magnitude sensitivity, topographic constraints, and societal responses, indicating that flood population exposure is shaped not only by hydrological processes but also strongly influenced by human decision-making and adaptive behavior[18,20]. Future growth in flood population exposure will remain closely related to population redistribution and socioeconomic development, rather than being driven

40 solely by changes in hazard itself[4,5,14].

41 Against this background, existing studies have provided substantial evidence for
42 the spatial inequality of flood exposure growth, floodplain population concentration,
43 and associated vulnerability[5,21–23]. However, systematic understanding remains limited
44 regarding the directional dynamics of population movement within high-risk flood
45 basins. This issue is particularly important because high-risk flood basins often face
46 both strong hazard pressure and strong economic attraction. Many such basins contain
47 fertile floodplains, major transport corridors, strategic coastal locations, dense urban
48 systems, and long-term development investment. Therefore, they may continue to
49 attract population inflows even under elevated hazard conditions[22,24]. Improvements in
50 protection can reduce the direct impacts of frequent flooding, but they may also
51 encourage additional settlement and asset accumulation in high-risk areas. This
52 phenomenon is commonly described as the "safe development paradox" or the "levee
53 effect"[10,20,25]. Under such circumstances, population exposure may continue to rise even
54 when flood-control capacity is strengthened. Meanwhile, development does not simply
55 reduce risk, but instead alters the balance between risk avoidance and place-based
56 attraction[24]. Broader migration research has further shown that population movement
57 under environmental stress is multi-causal and context dependent, and that it is jointly
58 shaped by hazard pressure, socioeconomic conditions, governance capacity, and
59 adaptive resources, rather than being attributable to climate or hazard alone[8,26–30].

60 This study revealed how population migration regimes in 520 major river basins

worldwide have shifted under the joint influence of flood exposure, relative flood-exposure vulnerability, and economic development. The analysis focused on 520 major basins across the globe during 1985–2021, with particular attention to long-term flood exposure, relative flood-exposure vulnerability, and basin-scale population redistribution. First, long-term flood activity intensity, relative population exposure, and their spatiotemporal variation were quantified at both pixel and basin scales, thereby characterizing the global pattern of flood occurrence and identifying where population exposure had increased most strongly over time. Second, the growth in population exposure was decomposed into the contributions of population growth, extreme rainfall, flood expansion, and their interaction, which made it possible to evaluate the relative importance of demographic and hydroclimatic drivers and to examine how these contributions vary along the economic gradient. Third, a basin-scale vulnerability assessment framework was developed by integrating persistent flood exposure, hydroclimatic pressure, and economic carrying capacity, thereby enabling the identification of basins where flood pressure and limited adaptive capacity are most strongly coupled. Finally, residual net migration was estimated separately for the early and late periods. Basins were then classified into five migration regimes. This classification enabled us to assess migration dynamics in major basins and further examine their relationships with vulnerability gradients and economic growth trajectories. This study reveals, from a basin-scale perspective, how risk, adaptation, and development interact to reshape human settlement dynamics in highly vulnerable

basins.

Exposure growth concentrates by basin

Between 1985 and 2021, flood population exposure was widespread across the globe, yet strongly concentrated within a limited subset of major river basins. Historical flood occurrence affected 65.7% of valid land pixels, but long-term population exposure, representing the persistent spatial overlap of human settlement and inundation, was more selective, occurring in 57.2% of pixels (the full global comparison is shown in Extended Data Fig. 1). This contrast shows that widespread flooding did not translate directly into equally widespread exposure. Instead, long-term exposure emerged primarily in areas where recurrent inundation repeatedly coincided with human occupation. Therefore, flood occurrence defined the broad hydrological footprint of flood-prone landscapes, whereas flood population exposure identified a narrower geography shaped by the sustained co-location of flooding and settlement. This distinction was also evident at the basin scale. Flood activity was globally extensive, but its burden was far from evenly distributed across the 520 major river basins. A relatively small number of large river systems accounted for a disproportionate share of both flood events and cumulative flood-affected area. The top 10 basins contributed 34.3% of all recorded events and 39.7% of cumulative flood-affected areas. This concentration was expressed in different ways: some basins stood out through repeated flood occurrence, whereas others were distinguished more by the accumulated spatial

extent of inundation. Flood frequency and cumulative affected area thus captured related, but not identical, dimensions of long-term flood activity (Fig. 1a).

Against this background, flood population exposure increased markedly over the study period, but its growth was highly uneven in both space and time. Positive changes occurred across 38.0% of valid land pixels, covering nearly 6×10^7 km², whereas negative changes were confined to only 4.0% of pixels (Fig. 1b). Contraction of flood population exposure was geographically limited, while growth dominated across a much larger share of the land surface. The temporal evolution shown in Fig. 1c further indicates that this increase did not follow a simple monotonic trajectory. Annual flooded area and annual exposed population both rose over the long term, but with clear multi-year fluctuations and two pronounced growth pulses. A first phase of increase extended from the late 1980s into the mid-1990s, when both flooded area and exposed population climbed from relatively low initial levels. This was followed by a period of weakening or partial decline from the late 1990s into the early 2000s. A second and more abrupt upswing then occurred in the early-to-mid 2000s, with both series reaching their highest values between 2003 and 2007. After this peak phase, both flooded area and exposed population declined from their maxima, but remained elevated relative to earlier decades and stabilized at comparatively high levels through the 2010s. The 5-year moving averages show the same overall pattern: a long-term upward trend expressed through alternating episodes of acceleration, decline, and renewed increase rather than through steady linear growth alone.

These temporal patterns were accompanied by strong basin-scale concentration. Recent exposure growth showed a distinctly top-heavy structure, with a small number of basins accounting for a large share of the global increase. The Ganges, Yangtze, and Indus alone contributed 31.5% of total positive exposure change, while the top 12 basins accounted for 55.3%. Even so, the recent increase remained more widely distributed than the long-term cumulative burden. When exposure was accumulated across the full 1985–2021 period, concentration became sharper: the Ganges, Yangtze, and Indus together represented 39.7% of total cumulative person-exposure, while the top 12 basins contributed 62.5% (Fig. 1d). Growth was therefore distributed across a broader set of basins, whereas cumulative burden remained anchored in fewer densely populated river systems, especially in South and Southeast Asia.

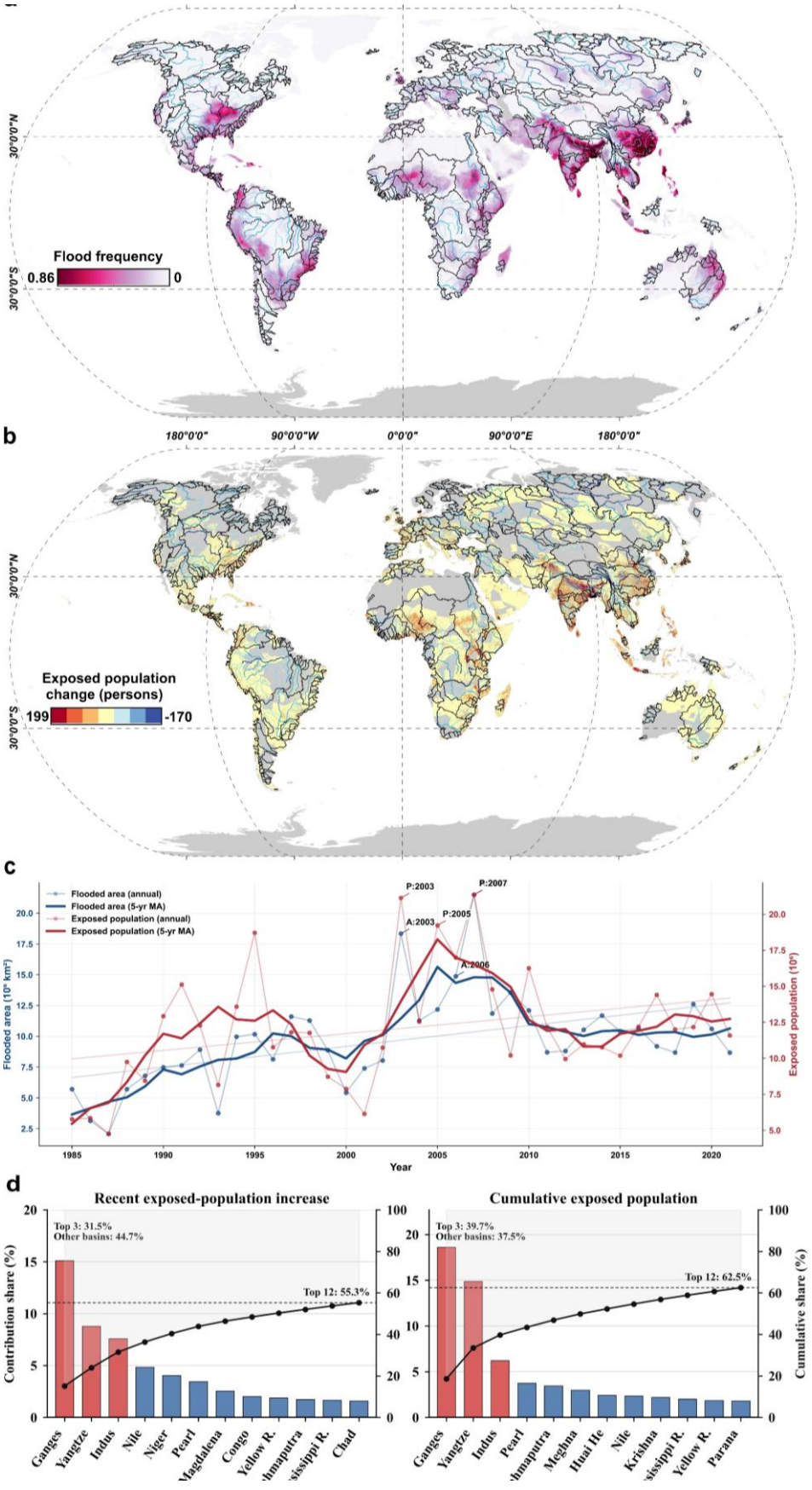


Fig. 1 Global flood exposure growth is spatially uneven and concentrated in major

river basins. a, Global flood frequency across 520 major river basins during 1985-2021. Flood frequency was calculated as the multi-year mean of annual flood occurrence for each valid pixel from annual DFO-derived flood masks; values range from 0, indicating no recorded flooding, to 1, indicating repeated flooding in every valid year. **b**, Pixel-scale change in exposed population between 1985 and 2021. **c**, Annual flooded area and exposed population during 1985-2021, with 5-year moving averages. **d**, Basin-level contribution shares and cumulative contribution curves for recent exposed-population increase and cumulative exposed population. The Ganges, Yangtze and Indus accounted for 31.5% of recent exposure increase, and the top 12 basins accounted for 55.3%; for cumulative exposed population, the corresponding shares were 39.7% and 62.5%.

Economic gradients of exposure growth

At the global scale, recent growth in flood population exposure was driven primarily by population growth, with flood expansion acting as the second most important contributor (Fig. 2a). Population growth accounted for 54.5% of total positive exposure increase, whereas flood expansion contributed 34.9%. By comparison, the joint effect of flood and population changes explained 6.5%, and extreme rainfall contributed only 4.1%. Recent exposure growth therefore remained dominated by demographic concentration in flood-prone areas, while hydrological change exerted its main influence through flood expansion rather than through extreme rainfall alone.

This global structure, however, varied strongly across the economic gradient (Fig. 2b,c). In low-GDP regions, exposure growth was overwhelmingly population-led.

Population growth contributed the largest absolute increase and accounted for 64.0% of total growth, whereas flood expansion represented only 27.7%. In middle-GDP regions, the dominance of population growth weakened and the contribution of flood expansion increased, narrowing the gap between the two. In high-GDP regions, the structure was reversed: flood expansion became the leading contributor, accounting for 58.3% of total exposure growth, while the contribution of population growth dropped to 15.8%. The joint effect and extreme rainfall also became relatively more important at the high-GDP end, indicating that exposure growth there was shaped by a broader mix of hydrological processes.

The spatial pattern of the attribution index was consistent with this economic differentiation. Regions such as the eastern United States, western Europe, Japan, Korea, and parts of eastern China were dominated by the non-population-growth side of the index, indicating that recent exposure increase in these areas was less strongly associated with continued demographic concentration and more closely related to hydroclimatic forcing. By contrast, eastern Europe, large parts of South America, much of Africa, India, and Southeast Asia were characterized by stronger population-growth dominance, showing that exposure expansion in these regions was more tightly linked to continued population increase and settlement concentration within flood-prone landscapes. The global geography of recent exposure growth was therefore not governed by a single process, but by a marked spatial division between population-led and more hydroclimatically influenced pathways. These economically differentiated

pathways of exposure growth reveal that persistent exposure pressure is filtered through unequal economic capacity, placing both into the same analytical frame and shifting the analysis from exposure increase alone to the geography of flood-exposure vulnerability.

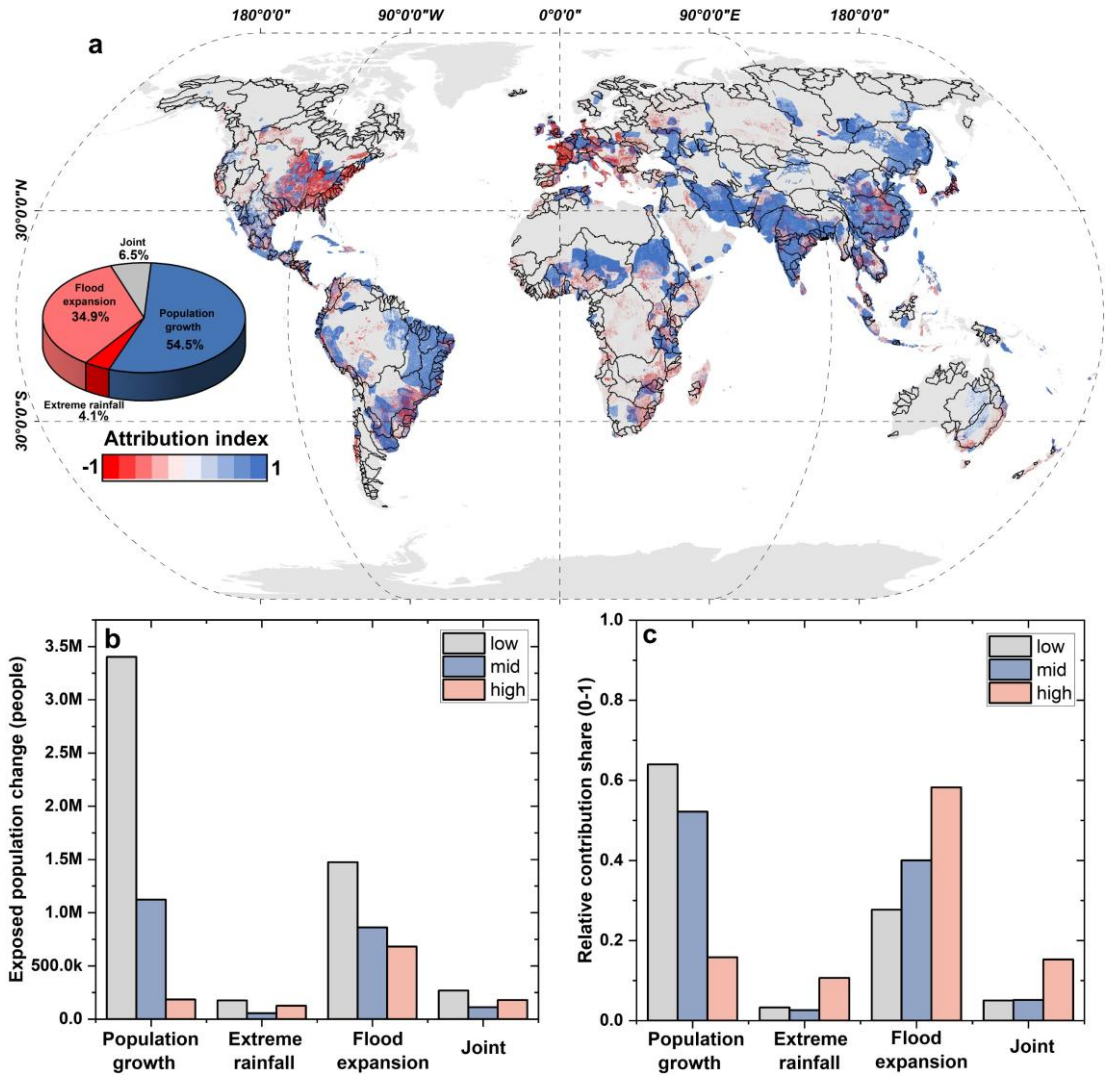


Fig. 2 Economic gradients shape the drivers of exposed-population growth. a, Spatial distribution of the attribution index comparing the relative dominance of population growth and extreme rainfall in exposed-population change; the inset summarizes the global contribution shares of population growth, extreme rainfall, flood expansion and their joint effect. **b**, Absolute exposed-population change attributed to the four components across low-, mid- and high-GDP groups. **c**, Relative contribution

189 shares of the same components across GDP groups. Bars show group-level totals, and
190 colours distinguish GDP groups.

191 **Exposure translates unevenly into vulnerability**

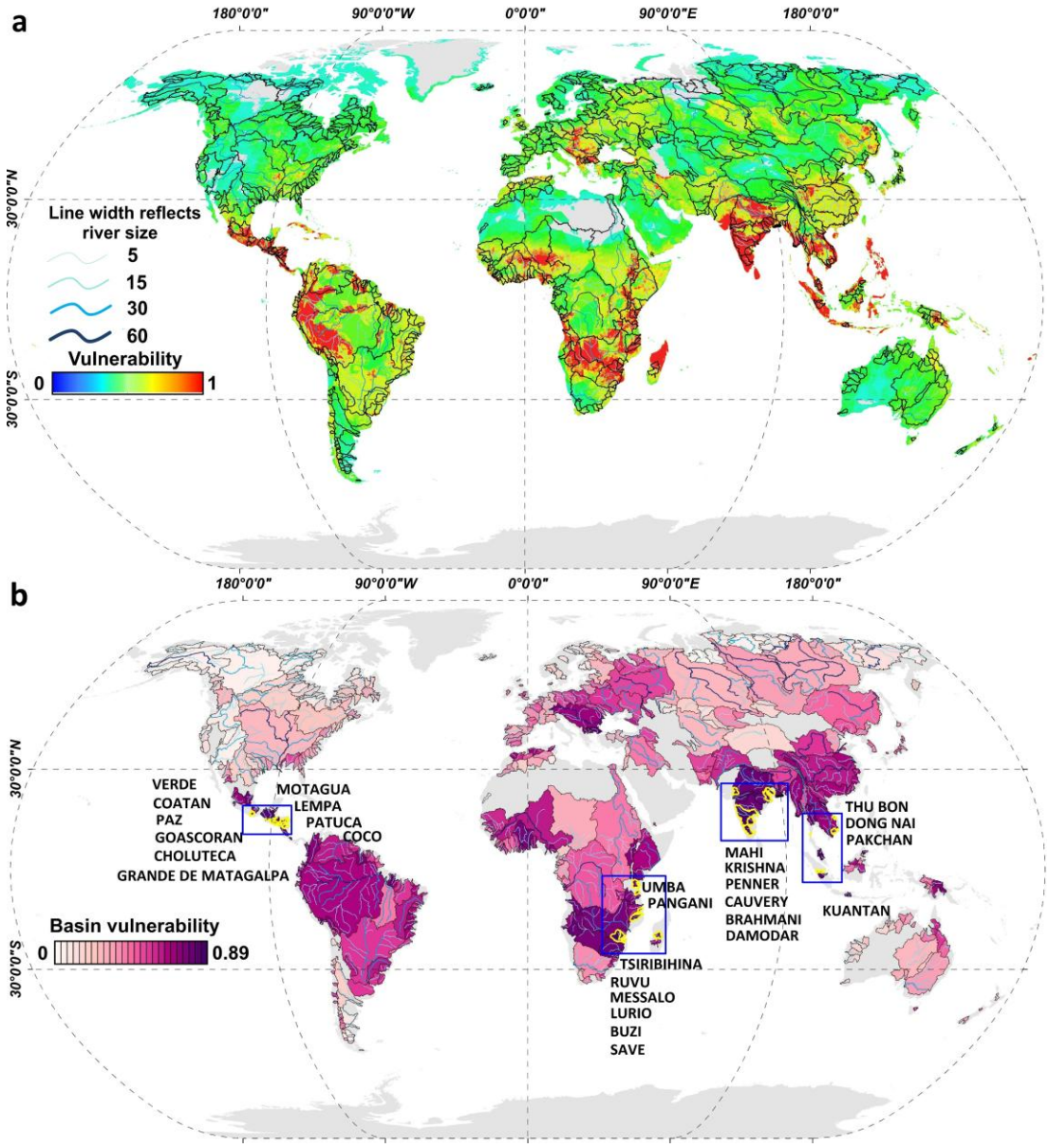
192 Relative flood-exposure vulnerability reveals a different global pattern from flood
193 activity or flood population exposure alone. Rather than estimating direct flood losses,
194 which remain difficult to represent consistently at the global scale, this framework
195 combines persistent flood-exposure pressure with GDP as a proxy for regional capacity
196 to support infrastructure, recover from disruption, and sustain longer-term adaptation[17].
197 Under this definition, relative flood-exposure vulnerability is not determined simply by
198 where flooding occurs or where the exposed population is large, but by where recurrent
199 flood pressure coincides with constrained economic capacity. Once regional capacity is
200 brought into the same frame as exposure pressure, the global geography of concern is
201 reordered rather than directly reproduced from the earlier patterns of flood frequency,
202 exposure change, or exposure attribution.

203 At the pixel scale, this produces a pattern that is widespread yet highly uneven.
204 Non-zero vulnerability occurs across 96.6% of valid pixels, but the highest values are
205 much more spatially selective, with the strongest concentrations extending across South
206 Asia, Southeast Asia, tropical Africa, parts of Central America, and several lowland
207 river corridors in South America (Fig. 3a). Large river belts, densely settled plains,
208 deltas, and tropical to subtropical flood-prone regions stand out most clearly. The
209 vulnerability surface does not simply mirror the earlier maps of flood frequency or

exposed-population growth. In China, especially in parts of the southeastern basin systems, flood frequency is relatively high and exposed population change is also marked, yet these basins do not rise into the highest global vulnerability class once regional capacity is incorporated. A similar contrast is visible in Japan, Korea, and parts of western Europe, where some basins remain hydrologically active and continue to register notable exposure growth, but their relative vulnerability is moderated to intermediate levels. By contrast, broad belts in South Asia, Southeast Asia, and tropical Africa retain relatively high values across recurrent flooding, exposure accumulation, and relative vulnerability, indicating that persistent exposure pressure is less effectively buffered in these settings. Relative vulnerability is therefore more selective than the geography of flood activity and more filtered than the geography of exposure growth.

This reordering becomes even clearer at the basin scale (Fig. 3b). The global mean area-weighted basin vulnerability is 0.504, but it rises to 0.882 for the 10 most vulnerable basins and remains 0.863 for the top 28, showing that the highest-vulnerability systems stand far above the global basin average. These basins are concentrated mainly in South Asia, Central America, and southeastern Africa, rather than being evenly distributed among the world's largest or most hydrologically prominent river systems. Specifically, in India, the Damodar, Mahi, Cauvery, and Krishna combine recurrent flood pressure, continued exposure accumulation, and high relative vulnerability within the same systems. In Honduras, El Salvador, Guatemala, and Nicaragua, another major cluster of high-vulnerability basins is formed by the Paz,

231 Goascoran, Motagua, Choluteca, and Grande de Matagalpa. Although this group of
232 basins is much less prominent than India in the global patterns of flood frequency and
233 exposure growth, it still contains a dense concentration of top-ranked vulnerable
234 systems. In Mozambique and Zimbabwe, the Buzi and Save also rise into the highest-
235 vulnerability group. What distinguishes these basins is the close alignment of recurrent
236 flood pressure, concentrated exposure, and constrained coping capacity. Basin
237 vulnerability therefore identifies not simply the places with the largest rivers or the
238 fastest exposure growth, but the basins where long-term flood-exposure pressure is least
239 absorbed by regional capacity.



240

241 **Fig. 3 Global pattern of flood-exposure vulnerability. a**, Pixel-scale flood-exposure

242 vulnerability, combining long-term population exposure, hydroclimatic pressure and

243 economic coping capacity. River line width indicates river size. **b**, Basin-scale mean

244 vulnerability across the 520 major river basins, with the most vulnerable basins

245 highlighted. Higher values indicate stronger co-location of population exposure and

246 flood-related pressure under weaker economic capacity.

Migration reversal in vulnerable basins

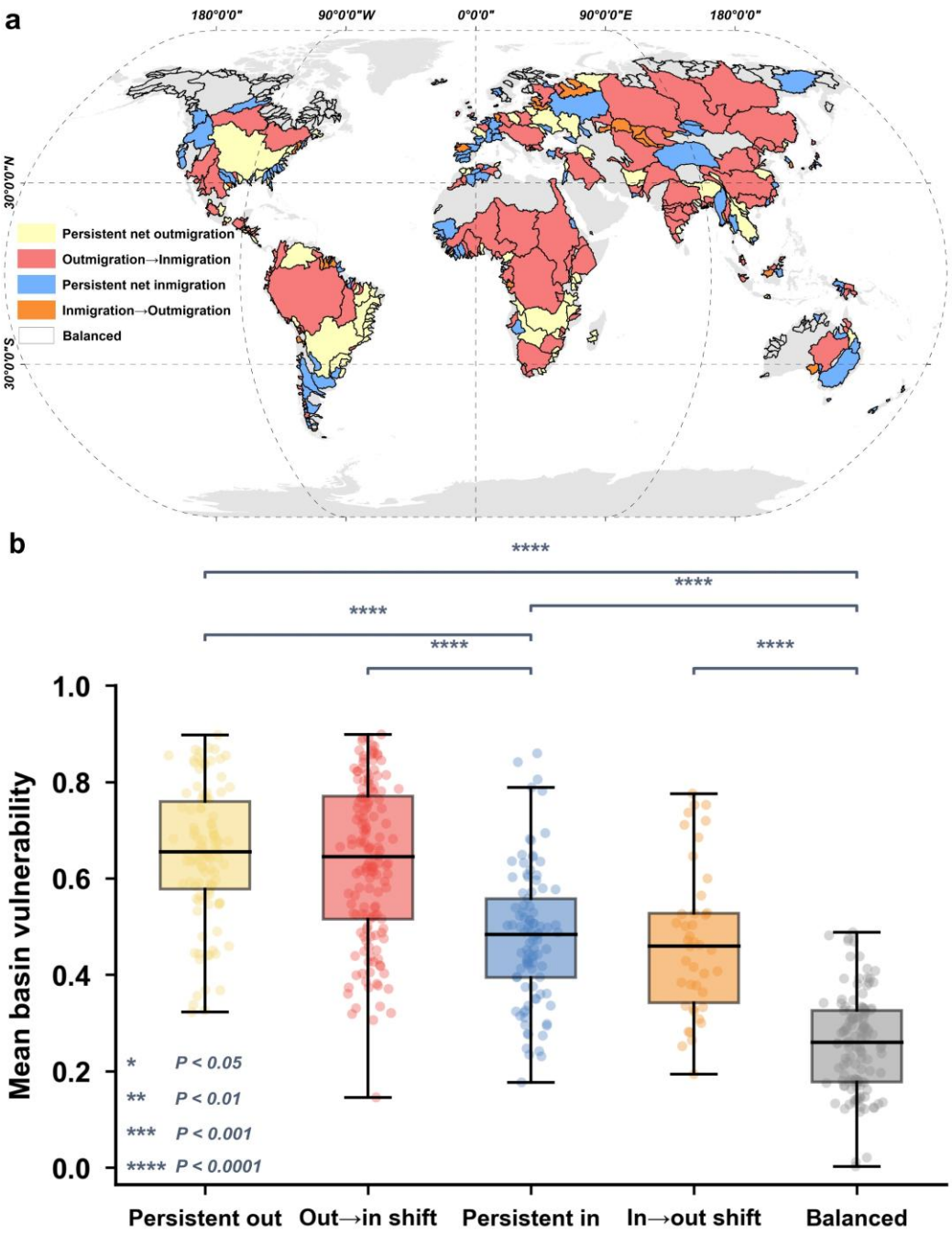
The migration results show that population dynamics in basins with high flood exposure are far more complex than a simple pattern of risk avoidance. If persistent flood pressure consistently translated into long-term demographic withdrawal, the dominant pathway should have been persistent net outmigration. Instead, the global distribution of migration regimes shows that basin trajectories are much more diverse, with both persistent net outmigration and out-to-in transition widely distributed across the 520 major river basins (Fig. 4a). This matters because the out-to-in regime is not confined to evidently low-pressure settings. Rather, it appears across basins where long-term flood-exposure pressure remains present, indicating that demographic responses to hazardous environments are not uniformly directional over time. The vulnerability structure of migration regimes reinforces this contrast(Fig. 4b). Basins in the out-to-in regime have a mean vulnerability of 0.633, which is very close to the 0.652 observed in basins with persistent net outmigration. Both values are substantially higher than those of persistent net inmigration (0.478), in-to-out (0.469), and weakly balanced basins (0.257). Elevated vulnerability is therefore compatible with at least two different migration trajectories: one in which the population continues to withdraw, and another in which earlier withdrawal gives way to later return. The key distinction is not whether vulnerability is high, but how populations respond to that condition over time.

Two typical examples illustrate this pattern. In the Pearl River Basin, our results identify an out-to-in migration regime, accompanied by high flood frequency in the

lower basin and Pearl River Delta, positive exposed-population change across many downstream urban areas, and elevated basin vulnerability (Extended Data Fig. 2). This interpretation is consistent with hydrological evidence showing that hazardous flood events are concentrated in the middle and lower Pearl River Basin, with marked changes in peak-flood processes mainly occurring during the late 1980s and 1990s[31]. At the same time, Guangdong and the Pearl River Delta have been widely recognized as major destinations for inter-provincial migration, driven by economic opportunity, industrialization, and urban employment growth[32]. A similar mechanism is evident in the Elbe River Basin, which is also classified as an out-to-in regime despite persistent flood-related pressure (Extended Data Fig. 3). The 2002 Elbe flood generated extreme discharge and severe losses[33]. Subsequent research shows that German flood-risk management was substantially reassessed after this event, including improvements in warning systems, emergency response, and integrated risk planning[34]. Together with renewed population growth in eastern German cities such as Dresden[35], this case supports the broader inference that development attraction and strengthened protection capacity can modify demographic responses to flood risk, offsetting earlier risk-avoidance signals.

Economic structure further differentiates these trajectories (Extended Data Fig. 4). Persistent net outmigration is dominated by low-GDP basins, which account for 60.4% of that regime. Persistent demographic withdrawal is more strongly associated with lower-development settings, whereas the transition from outmigration to inmigration

289 becomes more common as basin economic structure shifts upward. This relationship
290 becomes sharper when GDP growth is considered directly. Among all out-to-in basins,
291 46.31% belong to the high-GDP-growth group. Within the subset of highly vulnerable
292 out-to-in basins, that proportion rises to 70.69%. Here, high GDP growth is defined
293 from the upper tercile of the linear trend in log per-capita GDP during 1990–2021.
294 Rapid economic growth is therefore strongly represented in the same basins where
295 vulnerability remains high but migration shifts toward renewed inmigration. This does
296 not suggest that development removes flood pressure or fundamentally lowers
297 vulnerability. Rather, it indicates that stronger growth can alter the demographic
298 response to that pressure, making later population return more likely even under
299 persistently vulnerable conditions.



300

301 **Fig. 4 Migration regimes, economic structure, and mean basin vulnerability across**

302 **the 520 major river basins. a,** Global distribution of five basin migration regimes

303 classified from early- and late-period annual net migration rates: persistent net

304 outmigration, shift from outmigration to inmigration, persistent net inmigration, shift

305 from inmigration to outmigration and balanced. b, Mean basin vulnerability across

migration regimes. Boxes show the interquartile range, centre lines indicate medians, whiskers extend to 1.5 times the interquartile range and points represent individual basins. Significance was assessed using two-sided Mann-Whitney U tests; *P < 0.05, **P < 0.01, ***P < 0.001 and ****P < 0.0001.

Discussion

The differentiation of migration regimes suggests that population return in highly vulnerable basins is not accidental, but is associated with broader changes in development conditions. This finding extends previous studies showing that populations have not systematically retreated from highly vulnerable basins. Instead, both settlement extent and flood exposure in these basins have continued to expand, often faster than expected. This pattern is consistent with theoretical and systematic assessments emphasizing that migration under environmental stress is multi-causal and context dependent[7,36]. Global floodplain settlement patterns have likewise been shown to reflect both flood-magnitude sensitivity and societal adaptive capacity, with dense settlement remaining widespread even in areas exposed to rare but highly destructive floods[18]. Future increases in flood exposure are also expected to remain closely linked to population redistribution and socioeconomic development, rather than being driven solely by changes in hazard[4,14]. Within this broader context, our results add a demographic dimension by showing that economic development is not only associated with flood population exposure, but may also reshape migration pathways within highly vulnerable basins.

In the early stage, strong flood pressure, limited economic attraction, and weak local capacity are more likely to produce net outmigration. Under such conditions, repeated flooding acts mainly as a repelling force, while limited infrastructure, employment opportunities, public services, and recovery capacity reduce the incentive for settlement persistence or return. This pathway is most consistent with basins that remain in persistent net outmigration, where demographic withdrawal continues under conditions of elevated flood-exposure pressure and relatively weak development support. A different pathway emerges where economic growth is more rapid. In these basins, development does not eliminate flood pressure, but it changes the context within which populations respond to it. Improvements in infrastructure, governance capacity, flood protection, accessibility, and settlement conditions can reduce the disruptive effect of recurrent flooding on everyday life, while stronger economic growth enhances basin attractiveness through employment opportunities, urban expansion, land development, and the reconstruction of built environments. Population return then becomes more likely, even though flood-exposure pressure remains high, thereby intensifying flood population exposure in highly vulnerable basins (Fig. 5).

The safe development paradox provides a useful context for interpreting this process[37]. Flood-protection measures may reduce the impacts of frequent flooding while simultaneously attracting more people and assets into exposed areas[20]. Evidence from Bangladesh similarly shows that stronger structural flood protection can increase population density and asset concentration in protected flood-prone areas rather than

lead to long-term decline[38]. More broadly, migration responses to environmental stress are multi-causal and context dependent, shaped jointly by hazard pressure, livelihood opportunities, governance capacity, and adaptive resources, rather than by climate risk alone, the safe development paradox mechanisms operate in tandem with broader demographic and economic processes[7,36]. In this context, the present study suggests that economic development and improvements in flood-management capacity may help explain why some highly vulnerable basins shift from early net outmigration to later population return[17]. The key shift is therefore not from vulnerability to safety, but from flood pressure being the dominant demographic signal to a situation in which development-related attraction becomes strong enough to counterbalance earlier outmigration. In this sense, regional development no longer acts only as a condition that may reduce the impacts of flooding. In some highly vulnerable basins, it also becomes part of the process through which flood population exposure is rebuilt and further accumulated. These results also suggest that reducing flood risk in highly vulnerable basins cannot rely on engineering protection alone. More effective long-term management will require combining flood defenses with tighter land-use control and more careful guidance of settlement growth in areas where development and improved protection may otherwise reinforce renewed exposure accumulation.

At the same time, several uncertainties should be acknowledged. Migration regimes were inferred from residual net migration rather than directly observed bilateral migration flows. They therefore capture only the direction and relative intensity of net

redistribution, rather than specific origin–destination pathways. In addition, the vulnerability indicator was aggregated from the pixel scale to the basin scale. Although this approach is suitable for global comparison, it inevitably smooths local heterogeneity. Such scale-dependent simplification is common in large-scale flood assessments and has long been recognized as a source of uncertainty and bias[15,19]. Macro-scale indicators are useful for revealing broad global patterns, but they cannot fully represent localized adaptive behaviour, policy intervention, or finer human–flood feedbacks. These limitations do not overturn the main finding, but they indicate that the institutional and demographic pathways linking development, migration, and renewed flood population exposure should be examined more directly in future work.

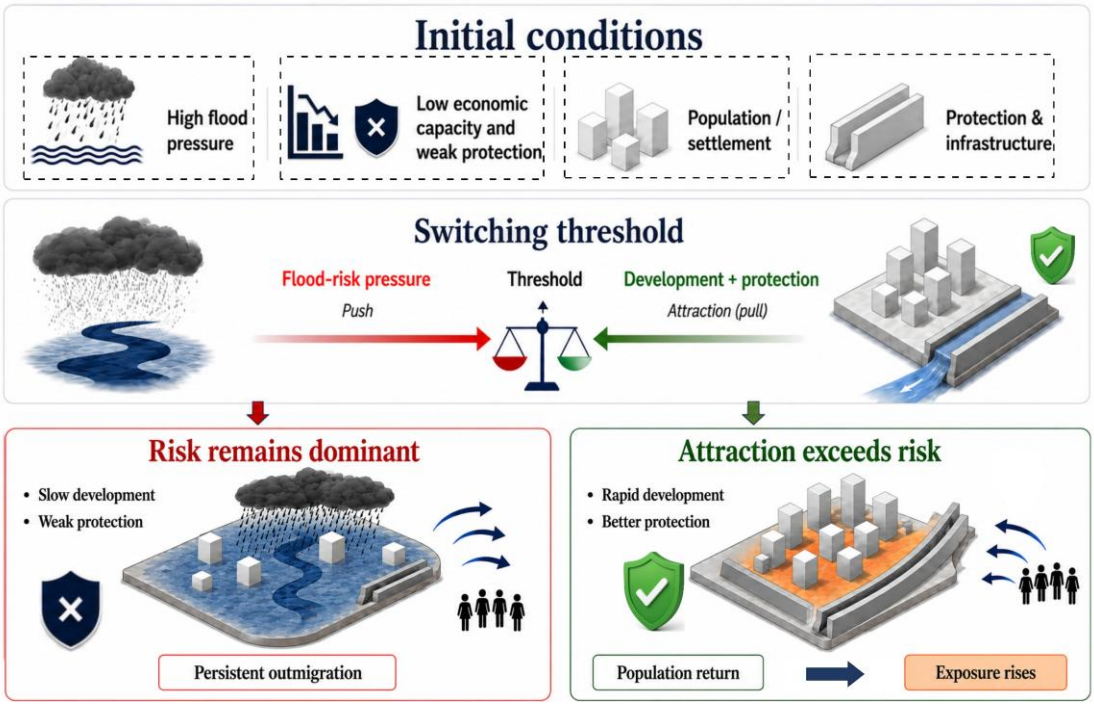


Fig. 5 Population migration pathways and flood exposure dynamics in highly vulnerable basins. Early population outmigration occurs in response to strong flood pressure and low economic attraction. Under slow economic development,

outmigration persists, local governance remains weak, and flood risk continues, leading to stagnation and low population exposure. In contrast, rapid economic growth improves governance and flood protection, enabling population return and the reconstruction of settlements, which in turn increases flood population exposure. These pathways illustrate how socioeconomic development and risk management jointly shape migration and long-term flood exposure patterns.

References

1. Tellman, B. *et al.* Satellite imaging reveals increased proportion of population exposed to floods. *Nature* **596**, 80–86 (2021).
2. Winsemius, H. C. *et al.* Global drivers of future river flood risk. *Nat. Clim. Chang.* **6**, 381–385 (2016).
3. Rentschler, J. *et al.* Global evidence of rapid urban growth in flood zones since 1985. *Nature* **622**, 87–92 (2023).
4. Rentschler, J., Salhab, M. & Jafino, B. A. Flood exposure and poverty in 188 countries. *Nat. Commun.* **13**, 3527 (2022).
5. Sauer, I. J. *et al.* Limited progress in global reduction of vulnerability to flood impacts over the past two decades. *Commun. Earth Environ.* **5**, 239 (2024).
6. Fox, S., Agyemang, F., Hawker, L. & Neal, J. Integrating social vulnerability into high-resolution global flood risk mapping. *Nat. Commun.* **15**, 3155 (2024).
7. Black, R., Bennett, S. R. G., Thomas, S. M. & Beddington, J. R. Climate change: Migration as adaptation. *Nature* **478**, 447–449 (2011).

8. Ronco, M. *et al.* Exploring interactions between socioeconomic context and natural hazards on human population displacement. *Nat. Commun.* **14**, 8004 (2023).
9. Mester, B., Frieler, K., Korup, O., Desai, B. & Schewe, J. Socioeconomic predictors of vulnerability to flood-induced displacement. *Nat. Commun.* **16**, 8296 (2025).
10. Di Baldassarre, G. *et al.* Debates - Perspectives on socio-hydrology: Capturing feedbacks between physical and social processes. *Water Resour. Res.* **51**, 4770–4781 (2015).
11. Jongman, B., Ward, P. J. & Aerts, J. C. J. H. Global exposure to river and coastal flooding: Long term trends and changes. *Glob. Environ. Chang.* **22**, 823–835 (2012).
12. Dottori, F. *et al.* Increased human and economic losses from river flooding with anthropogenic warming. *Nat. Clim. Chang.* **8**, 781–786 (2018).
13. Hallegatte, S., Green, C., Nicholls, R. J. & Corfee-Morlot, J. Future flood losses in major coastal cities. *Nat. Clim. Chang.* **3**, 802–806 (2013).
14. Rogers, J. S., Maneta, M. M., Sain, S. R., Madaus, L. E. & Hacker, J. P. The role of climate and population change in global flood exposure and vulnerability. *Nat. Commun.* **16**, 1287 (2025).
15. de Moel, H. *et al.* Flood risk assessments at different spatial scales. *Mitig. Adapt. Strateg. Glob. Chang.* **20**, 865–890 (2015).

16. Wing, O. E. J. *et al.* Inequitable patterns of US flood risk in the Anthropocene. *Nat. Clim. Chang.* **12**, 156–162 (2022).
17. Fan, J. *et al.* Exploring how economic level drives urban flood risk. *Nat. Commun.* **16**, 4857 (2025).
18. Devitt, L., Neal, J., Coxon, G., Savage, J. & Wagener, T. Flood hazard potential reveals global floodplain settlement patterns. *Nat. Commun.* **14**, 2801 (2023).
19. Hinkel, J. *et al.* Uncertainty and Bias in Global to Regional Scale Assessments of Current and Future Coastal Flood Risk. *Earth's Futur.* **9**, e2020EF001882 (2021).
20. Burby, R. J. Hurricane Katrina and the Paradoxes of Government Disaster Policy: Bringing About Wise Governmental Decisions for Hazardous Areas. *Ann. Am. Acad. Pol. Soc. Sci.* **604**, 171–191 (2006).
21. McDermott, T. K. J. Global exposure to flood risk and poverty. *Nat. Commun.* **13**, 3529 (2022).
22. Mazzoleni, M. *et al.* Floodplains in the Anthropocene: A Global Analysis of the Interplay Between Human Population, Built Environment, and Flood Severity. *Water Resour. Res.* **57**, e2020WR027744 (2021).
23. Varis, O., Taka, M. & Tortajada, C. Global human exposure to urban riverine floods and storms. *River* **1**, 80–90 (2022).
24. Wang, Y. *et al.* Development policy affects coastal flood exposure in China more than sea-level rise. *Nat. Clim. Chang.* **15**, 1071–1077 (2025).
25. Baldassarre, G. Di *et al.* Hess opinions: An interdisciplinary research agenda to

explore the unintended consequences of structural flood protection. *Hydrol. Earth Syst. Sci.* **22**, 5629–5637 (2018).

26. Schutte, S., Vestby, J., Carling, J. & Buhaug, H. Climatic conditions are weak predictors of asylum migration. *Nat. Commun.* **12**, 2067 (2021).

27. Benveniste, H., Huybers, P. & Proctor, J. Global climate migration is a story of who and not just how many. *Nat. Commun.* **16**, 7752 (2025).

28. Piguet, E. Linking climate change, environmental degradation, and migration: An update after 10 years. *Wiley Interdiscip. Rev. Clim. Chang.* **13**, e746 (2022).

29. Nabong, E. C., Hocking, L., Opdyke, A. & Walters, J. P. Decision-making factor interactions influencing climate migration: A systems-based systematic review. *Wiley Interdiscip. Rev. Clim. Chang.* **14**, e828 (2023).

30. Daoust, G. & Selby, J. Climate change and migration: A review and new framework for analysis. *Wiley Interdiscip. Rev. Clim. Chang.* **15**, e886 (2024).

31. Zhang, Q., Gu, X., Singh, V. P., Shi, P. & Sun, P. More frequent flooding? Changes in flood frequency in the Pearl River basin, China, since 1951 and over the past 1000 years. *Hydrol. Earth Syst. Sci.* **22**, 2637–2653 (2018).

32. Cindy Fan, C. Economic opportunities and internal migration: A case study of guangdong province, China. *Prof. Geogr.* **48**, 28–45 (1996).

33. Büchele, B. *et al.* Flood-risk mapping: Contributions towards an enhanced assessment of extreme events and associated risks. *Nat. Hazards Earth Syst. Sci.* **6**, 483–503 (2006).

34. KREIBICH, H. & MERZ, B. Lessons Learned From the Elbe River Floods in August 2002 - With a Special Focus on Flood Warning. *Extrem. Hydrol. Events New Concepts Secur.* 69–80 (2007) doi:10.1007/978-1-4020-5741-0_5.

35. Wolff, M., Haase, A., Leibert, T. & Cunningham Sabot, E. Calm ocean or raging sea? Tracing 30 years of demographic and spatial development in Germany. *CyberGeo* **2022**, (2022).

36. Hoffmann, R., Šedová, B. & Vinke, K. Improving the evidence base: A methodological review of the quantitative climate migration literature. *Glob. Environ. Chang.* **71**, 102367 (2021).

37. Fusinato, E., Han, S., Kobiyama, M. & de Brito, M. M. Safe development paradox: evidence and methodological insights from a systematic review. *Nat. Hazards* **120**, 13693–13714 (2024).

38. Ferdous, M. R., Di Baldassarre, G., Brandimarte, L. & Wesselink, A. The interplay between structural flood protection, population density, and flood mortality along the Jamuna River, Bangladesh. *Reg. Environ. Chang.* **20**, 5 (2020).

39. Pesaresi, M. *et al.* Advances on the global human settlement layer by joint assessment of earth observation and population survey data. *Int. J. Digit. Earth* **17**, 2390454 (2024).

40. Tatem, A. J. WorldPop, open data for spatial demography. *Sci. Data* **4**, 170004 (2017).

41. Muñoz-Sabater, J. *et al.* ERA5-Land: A state-of-the-art global reanalysis dataset

for land applications. *Earth Syst. Sci. Data* **13**, 4349–4383 (2021).

42. Kummu, M., Kosonen, M. & Masoumzadeh Sayyar, S. Downscaled gridded global dataset for gross domestic product (GDP) per capita PPP over 1990–2022. *Sci. Data* **12**, 178 (2025).

Methods

Reconstruction of annual population surfaces

To construct a globally consistent annual population dataset for 1985–2021, we integrated the Global Human Settlement Layer[39] and WorldPop population products[40] on a common 1 km grid. The GHSL dataset provides temporally consistent benchmark population surfaces for 1985, 1990, 1995, 2000, 2005, 2010, 2015 and 2020, whereas WorldPop provides annual population estimates for 2000- 2020. Both products were first mosaicked year by year from their original global tiles, and all rasters were harmonized to a common 1-km population grid used by the reconstructed annual population product.

For 1985–1999, the annual population was reconstructed by linear interpolation between adjacent GHSL benchmark years. For a target year y lying between benchmark years a_0 and a_1, the population was estimated as:

$$P_y = (1-\alpha)G_{a0} + \alpha G_{a1} \quad (1)$$

where G_{a0} and G_{a1} are the GHSL population counts for the two benchmark years, and

$$\alpha = \frac{y - a_0}{a_1 - a_0} \quad (2)$$

For 2000–2020, the annual population was estimated by applying a GHSL-based correction factor to the WorldPop annual population. At each GHSL benchmark year, a calibration ratio was defined as:

$$R_a = \frac{G_a}{W_a} \quad (3)$$

where G_a and W_a are GHSL and WorldPop population counts for the same benchmark

year. To avoid instability caused by very small denominators, the ratio was constrained within a predefined interval:

$$R_a^* = \min\left(R_{max}, \max\left(R_{min}, R_a\right)\right) \quad (4)$$

For a target year y between two benchmark years a_0 and a_1, the correction factor was linearly interpolated as:

$$R_y = (1-\alpha)R_{a0}^* + \alpha R_{a1}^* \quad (5)$$

Annual population was then reconstructed as:

$$P_y = W_y \cdot R_y \quad (6)$$

where W_y is the WorldPop annual population surface for year y. For 2021, the 2020 calibrated ratio was carried forward, such that:

$$P_{2021} = W_{2020} \cdot R_{2020}^* \quad (7)$$

All negative values and invalid cells were treated as missing data and excluded from subsequent analyses. This reconstruction strategy preserved the long-term structural consistency of GHSL while retaining the year-to-year variability represented by WorldPop.

Derivation of annual extreme rainfall indices

Annual extreme rainfall indices were derived from ERA5-Land daily aggregated data[41] in Google Earth Engine. Daily rainfall was calculated by subtracting snowfall water equivalent from total precipitation and converting the result to millimetres per day:

$$Rain_d = \max\left[0, 1000(TP_d - SF_d)\right] \quad (8)$$

where TP_d and SF_d are daily total precipitation and snowfall, respectively, expressed

in metres of water equivalent. This treatment was used to isolate liquid rainfall relevant to flood generation and to exclude snowfall contributions. Wet days were defined as days with daily rainfall greater than or equal to 1 mm. Using all wet-day rainfall values during the reference period 1950–1979, a pixel-wise 90th percentile threshold was computed. The contribution of extreme rainfall to annual wet-day precipitation was computed as:

$$R90pTOT_y = 100 \times \frac{\sum_{d \in y} Rain_d \cdot I(Rain_d \geq 1 \cap Rain_d > P_{90})}{\sum_{d \in y} Rain_d \cdot I(Rain_d \geq 1)} \quad (9)$$

Flood footprint construction and flood frequency estimation

Annual population exposure at the pixel scale was estimated by integrating annual flood masks with spatially explicit annual population datasets. This approach quantifies the number of individuals residing within inundated areas in each year. For multi-period analyses, the mean population values were first calculated for both the baseline and the late periods. The corresponding population exposure was then derived for each period. The net change in population exposure between the two periods was determined as the difference between the late-period and baseline-period estimates. This analytical framework provides a globally consistent metric for assessing long-term changes in population exposure, accounting for both spatiotemporal variations in flood occurrence and shifts in population distribution.

Treatment of spatial heterogeneity and scale transition

To ensure consistency across multi-source datasets while preserving local variation, all analyses were referenced to the geometry of the 1985 annual population raster, which

served as the common 1 km analysis grid. Annual population surfaces for 1985–2021 were reconstructed on this grid by integrating GHSL benchmark layers and WorldPop annual estimates, so population was directly available in a unified pixel framework. Annual flood occurrence was not derived from a pre-existing raster product, but was generated by rasterizing DFO flood polygons to the same template grid year by year, allowing flood masks and flood-exposed population to be calculated directly at the pixel scale. Extreme-rainfall rasters were read annually and, where necessary, reprojected to the template grid at the block level using bilinear resampling, whereas the GDP per capita dataset was first summarized at its native multi-band coarse resolution to derive a multi-year mean surface and was then reprojected to the 1 km template grid. GDP was used as a relative proxy for regional coping capacity rather than as a fine-scale local socioeconomic measurement. Spatial heterogeneity was handled through a pixel-first analytical design, in which flood frequency, relative exposure, attribution components, and relative flood-exposure vulnerability were first calculated at the pixel scale to retain local variation in flood occurrence, exposed population, rainfall pressure, and economic capacity, and only then summarized within HydroBASINS basin boundaries for basin-scale comparison. To improve comparability across regions with strongly unequal hydroclimatic and demographic conditions, variables with pronounced right-skewness, including population growth pressure, mean extreme rainfall, and positive extreme-rainfall trend, were transformed using $\ln(1+x)$ before robust quantile normalization. This procedure did not remove spatial heterogeneity itself, but reduced the dominance

of local extremes in cross-regional comparison. Under this framework, scale conversion was minimized where possible, and when necessary it was implemented explicitly within a common spatial reference system tied to the annual population template, so that local heterogeneity was preserved during indicator construction before being synthesized at the basin scale.

Attribution of population exposure change

To quantify the relative roles of demographic growth, extreme rainfall, and flood change in shaping the increase in population exposure, we developed a pixel-wise attribution framework based on baseline and late-period flood frequency, population, and extreme rainfall. Population exposure was defined as the product of flood occurrence and population. Accordingly, the observed changes in flood frequency and mean population between the late and baseline periods were first calculated as:

$$\begin{cases} dF_{obs} = F_l - F_b \\ dP = P_l - P_b \end{cases} \tag{10}$$

where F_b and F_l are the baseline- and late-period flood frequencies, respectively, and P_b and P_l are the corresponding baseline and late-period mean population. To isolate the component of flood change associated with extreme rainfall, we estimated a pixel-wise linear relationship between annual flood occurrence and annual extreme rainfall amount over 1985–2021:

$$F_y = a \cdot \beta R_y \tag{11}$$

where F_y is the annual flood occurrence, R_y is the annual extreme rainfall amount, and β is the fitted regression coefficient. Based on this relationship, the flood-frequency

598 change associated with extreme rainfall was estimated as:

599 $$dF_{ext} = \beta(R_l - R_b) \quad (12)$$

600 where R_b and R_l are the baseline and late-period means of annual extreme rainfall
601 amount, respectively. The remaining component of flood change, representing the
602 portion of observed flood frequency/extent change not explained by extreme rainfall,
603 was defined as:

604 $$dF_{flood} = dF_{obs} - dF_{ext} \quad (13)$$

605 This term reflects the residual change in mapped flood occurrence, including the
606 integrated effects of flood expansion or contraction and flood-frequency variation
607 beyond the contribution explained by extreme rainfall. Population exposure change was
608 then decomposed into four attribution components:

609 $$\begin{cases} dPE_{pop} = F_b \cdot dP \\ dPE_{ext} = dF_{ext} \cdot P_b \\ dPE_{flood} = dF_{flood} \cdot P_b \\ dPE_{joint} = dF_{obs} \cdot dP \\ dPE = dPE_{pop} + dPE_{ext} + dPE_{flood} + dPE_{joint} \end{cases} \quad (14)$$

610 In this formulation, dPE_{pop} represents the contribution of population growth
611 under baseline flood conditions, dPE_{ext} represents the contribution of extreme-
612 rainfall-driven flood change, dPE_{flood} represents the contribution of residual flood
613 expansion/frequency change not explained by extreme rainfall, and dPE_{joint} represents
614 the interaction between flood change and population change. To compare the relative
615 dominance of demographic and climatic controls, we further defined a normalized
616 attribution index as:

$$I_{pop-ext} = \frac{dPE_{pop} - dPE_{ext}}{|dPE_{pop}| + |dPE_{ext}| + |dPE_{flood}| + |dPE_{joint}| + \varepsilon} \quad (15)$$

where ε is a small constant introduced to avoid division by zero. Positive values indicate that population growth contributed more strongly than extreme rainfall to the increase in population exposure, whereas negative values indicate stronger dominance of extreme rainfall.

GDP-stratified attribution analysis

To examine whether the drivers of population exposure change differed across socioeconomic settings, we used the gridded GDP per capita dataset to construct a multi-year socioeconomic capacity layer[42]. Annual GDP per capita rasters were first averaged over the selected analysis period and then resampled to the common 1 km grid. To reduce distributional skewness, the GDP per capita values were log-transformed before further analysis. The transformed GDP surface was subsequently divided into low-, middle-, and high-GDP terciles according to the global distribution of valid pixels. Within each GDP group, the positive values of total exposure change and its four attribution components, including the population-growth term, extreme-rainfall term, flood expansion/frequency change term, and joint term, were summed to compare how the relative importance of demographic growth and hydroclimatic forcing varied across socioeconomic levels. The resulting grouped statistics were used to quantify both the absolute magnitude and the relative contribution of each attribution component along the economic gradient.

Relative flood-exposure vulnerability assessment

A relative flood-exposure vulnerability assessment index was constructed by integrating long-term flood exposure, population growth in flood-affected areas, extreme rainfall pressure, extreme rainfall trend, and local economic capacity. The land mask was defined from the reconstructed 1985 population raster, retaining all finite and non-negative land cells and excluding ocean pixels.

Relative exposure was first calculated from the annual flood masks derived from the DFO archive and the reconstructed annual population surfaces as：

$$RE = \frac{\sum_{y=1985}^{2021} M_y P_y}{\sum_{y=1985}^{2021} M_y} \tag{16}$$

where M_y is the annual flood mask and P_y is the annual population. This term describes the long-term fraction of the cumulative population located within mapped flood footprints.

Population growth pressure in flood-affected areas was then estimated from the difference between the mean population in the baseline period (1985–1989) and the late period (2017–2021). Only positive growth was retained, and this component was weighted by long-term flood frequency:

$$PG = FF \cdot \frac{\max\left(P_{late} - P_{base}, 0\right)}{P_{base}} \tag{17}$$

where P_{base} and P_{late} denote the mean population in the two periods, and FF is the long-term flood frequency over 1985–2021.

Extreme rainfall pressure was characterized using the multi-year mean of annual extreme rainfall amount:

$$RM = \frac{1}{n}\sum_{y=1985}^{2021} R_y \quad (18)$$

where R_y is the annual extreme rainfall amount and n is the number of valid years.

The long-term intensification of extreme rainfall was represented by the positive linear trend of annual extreme rainfall amount:

$$RT = \max(s_R, 0) \quad (19)$$

where s_R is the slope of the annual extreme rainfall amount series over 1985–2021.

To place these indicators on a comparable scale, robust quantile normalization was applied to each component. For strongly right-skewed variables, including PG, RM, and RT, a $ln(1+x)$ transformation was applied before normalization. The normalized exposure and hydroclimatic components were then combined into a composite hazard-pressure term:

$$H = aS_{RE} + bS_{PG} + cS_{RM} + dS_{RT} \quad (20)$$

where S_{RE}, S_{RE}, S_{RE}, and S_{RE} are the normalized component scores, and a, b, c, and d are their corresponding weights.

Economic coping capacity was represented using the normalized log-transformed GDP per capita surface. Low economic capacity was defined as the inverse of the normalized GDP score, and the final relative vulnerability index was calculated as:

$$V = LowGDP \cdot H \quad (21)$$

Under this framework, higher vulnerability is assigned to locations where long-term flood exposure and hydroclimatic pressure are high while economic capacity is low.

Basin-scale migration regime identification

For each basin, population totals were extracted from annual gridded population data at both the beginning and the end of each period. Population change during a given period was calculated as：

$$\Delta P = P_{end} - P_{start} \tag{22}$$

where P_{start} and P_{end} denote the basin population at the beginning and end of the period, respectively.

Natural increase was estimated from annual crude birth rates (CBR) and crude death rates (CDR). Basin populations were linked to country-level demographic rates through basin-country units, and annual natural increase was calculated as

$$NI = \sum_{t=1}^{T} P_t \frac{CBR_t - CDR_t}{1000} \tag{23}$$

where P_t is the basin population in year t, and T is the number of years in the period. Residual net migration was then derived from the population accounting identity as:

$$NM = (P_{end} - P_{start}) - NI \tag{24}$$

where NM>0 indicates net inmigration and NM <0 indicates net outmigration. Because the early and late periods differ in duration, migration intensity was further standardized as an annualized residual net migration rate:

$$ANMR = \frac{NM}{P_{start} \times T} \times 100 \tag{25}$$

where $ANMR$ is expressed in % yr^{-1}. In the present study, the sign of NM was used to determine migration direction, whereas $ANMR$ was used to compare migration intensity between periods.

Data availability

The HydroBASINS basin boundaries used in this study are available at https://www.hydrosheds.org/products/hydrobasins. The GHS-POP R2023A population grids are available from the Global Human Settlement Layer product page at https://human-settlement.emergency.copernicus.eu/ghs_pop2023.php and are mirrored in the Google Earth Engine data catalogue at https://developers.google.com/earth-engine/datasets/catalog/JRC_GHSL_P2023A_GHS_POP. The WorldPop Global1 population datasets used for annual population reconstruction are available at https://hub.worldpop.org/Global1_2000-2020. The ERA5-Land daily aggregated data used to derive annual extreme rainfall indices are available from the Copernicus Climate Data Store at https://cds.climate.copernicus.eu/datasets/reanalysis-era5-land and are mirrored in the Google Earth Engine data catalogue at https://developers.google.com/earth-engine/datasets/catalog/ECMWF_ERA5_LAND_DAILY_AGGR. The Dartmouth Flood Observatory flood records used to construct annual flood masks and flood frequency metrics are available at https://floodobservatory.colorado.edu/wiki/FloodRecords. The gridded GDP per capita dataset used for the economic-gradient and vulnerability analyses is available at https://zenodo.org/records/16741980, and the latest version of the dataset is available at https://zenodo.org/records/10976734/latest. The crude birth rate and crude death rate data used in the migration analysis are available from the World Bank indicator pages

721 at https://data.worldbank.org/indicator/SP.DYN.CBRT.IN. The annual population
722 surfaces, annual extreme rainfall indices, basin-scale exposure metrics, vulnerability
723 estimates, and migration-regime classification tables generated in this study are
724 available from the corresponding author upon reasonable request.

725 **Code availability**

726 The core analysis code for population exposure, flood vulnerability and migration-
727 regime classification is available on Zenodo at
728 https://doi.org/10.5281/zenodo.20587183.

729 **Acknowledgements**

730 This work was supported by the Key Special Project of Technological Innovation and
731 Application Development of Chongqing, No. CSTB2025TIAD-KPX0032.

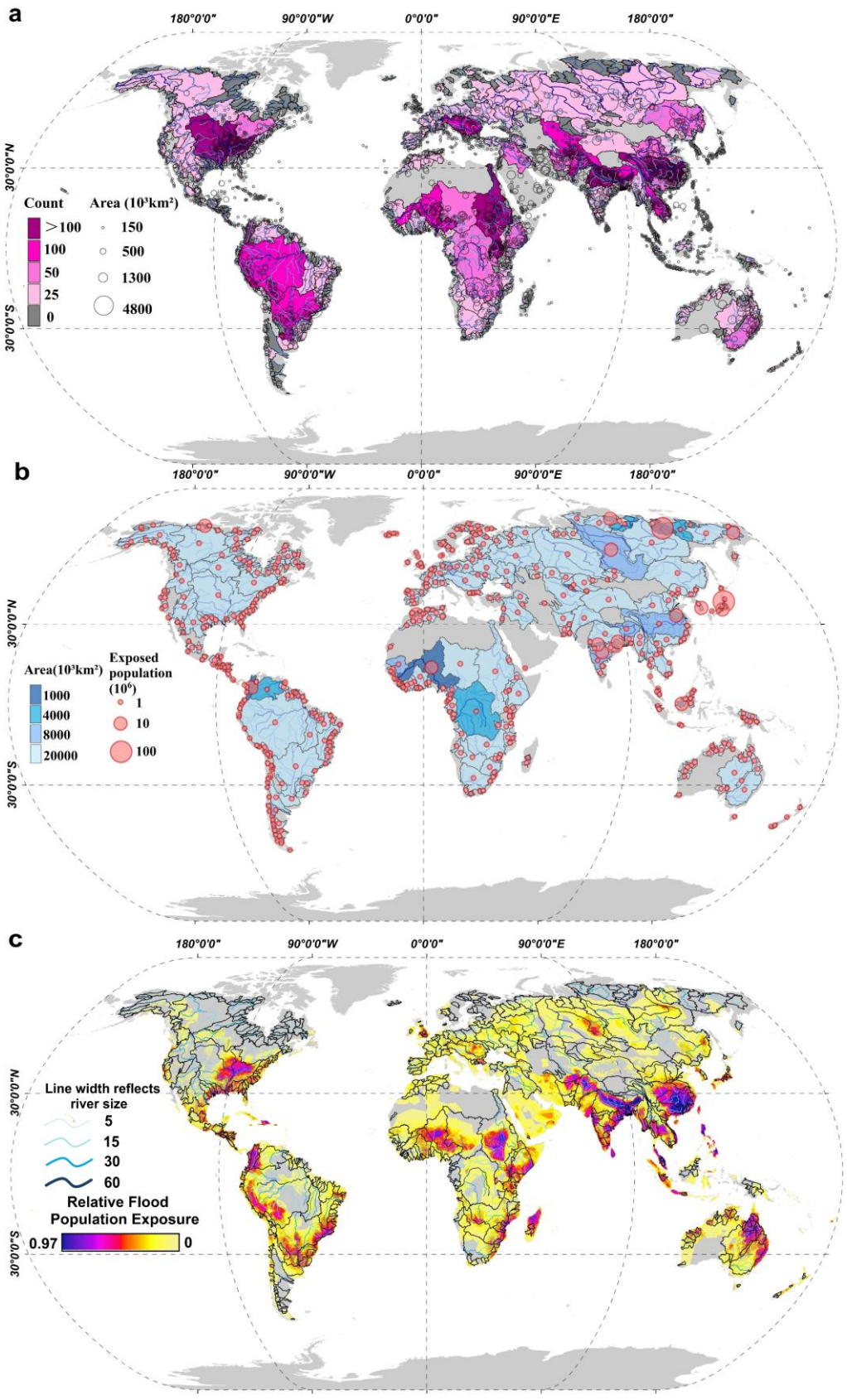
732 **Author contributions**

733 A.J. and H.Y. conceived the study. A.J. designed the analytical framework, processed
734 the geospatial and demographic datasets, performed the flood-exposure, vulnerability,
735 attribution and migration-regime analyses, generated the figures and wrote the initial
736 manuscript draft. X.L. contributed to data processing, figure preparation and
737 interpretation of the exposure-attribution results. Z.J. contributed to methodological
738 discussion, interpretation of flood-risk and vulnerability patterns, and manuscript
739 revision. L.P. contributed to the interpretation of socioeconomic and migration-related
740 results and provided comments on the manuscript. H.Y. supervised the study, guided
741 the research design and interpretation, and revised the manuscript. All authors discussed

the results and approved the final manuscript.

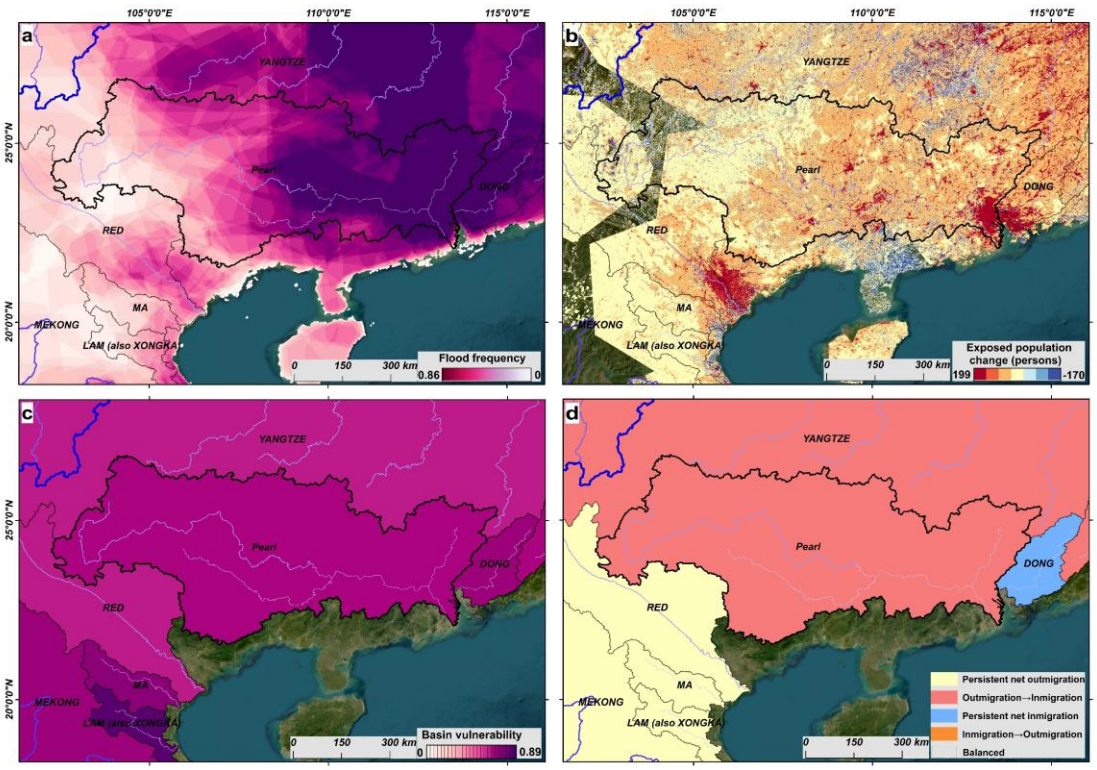
Competing interests

The authors declare no competing interests.



Extended Data Fig. 1 Global flood activity and long-term population exposure across 520 major river basins. a, Basin-scale flood event count and cumulative flood-

affected area during 1985-2021. Across the full archive, 3,152 flood events were identified, and the top 10 basins accounted for 34.3% of all events. The Mississippi, Yangtze, Nile and Ganges each recorded more than 120 events, with the Danube and Amazon also among the most active systems. **b**, Basin-scale relationship between cumulative flood-affected area and total flood-exposed population, showing that flood activity and population exposure were concentrated in a limited number of large river systems. **c**, Pixel-scale relative exposure, representing the long-term co-location of flood occurrence and population. Non-zero relative exposure occurred in 57.2% of valid pixels, corresponding to approximately 8.91×10^7 km^2, or 65.1% of valid land area. The distribution was strongly right-skewed, with a mean of 0.0838, median of 0.0351, 90th percentile of 0.242, 95th percentile of 0.331 and 99th percentile of 0.507.



760

761 **Extended Data Fig. 2 Spatial evidence of migration regime reversal in the Pearl**

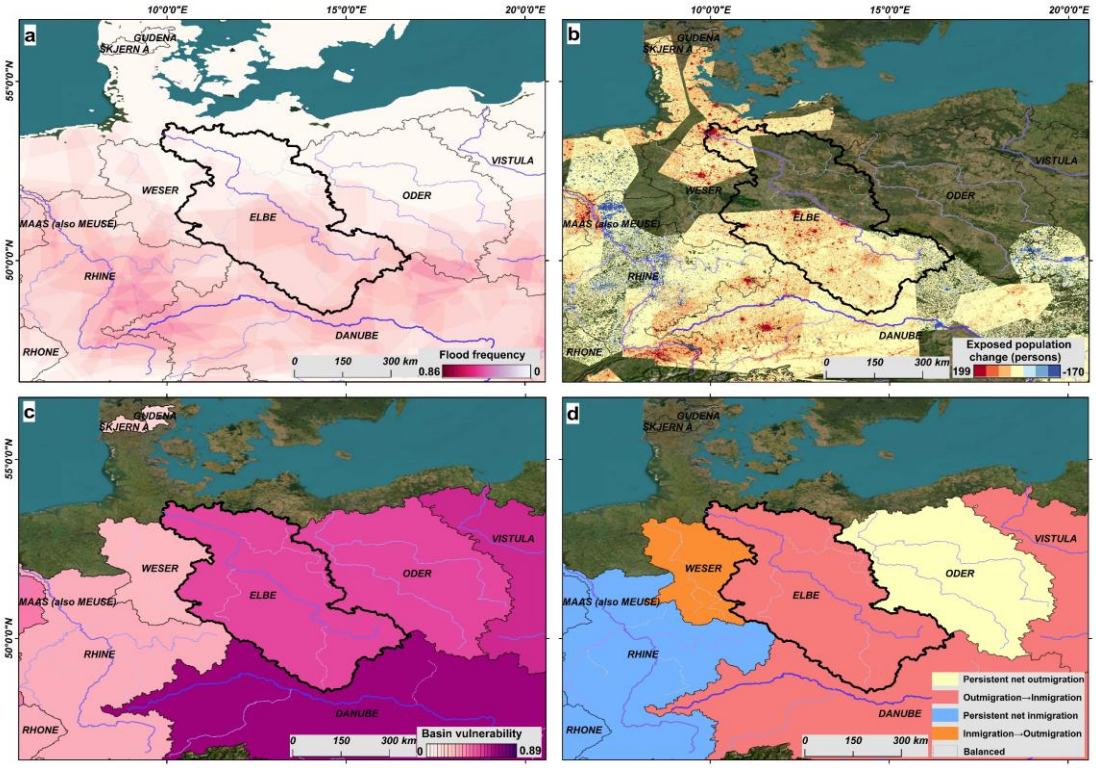
762 **River Basin. a**, Flood frequency in and around the Pearl River Basin during 1985-2021.

763 **b**, Pixel-scale exposed-population change. **c**, Basin vulnerability, with higher values

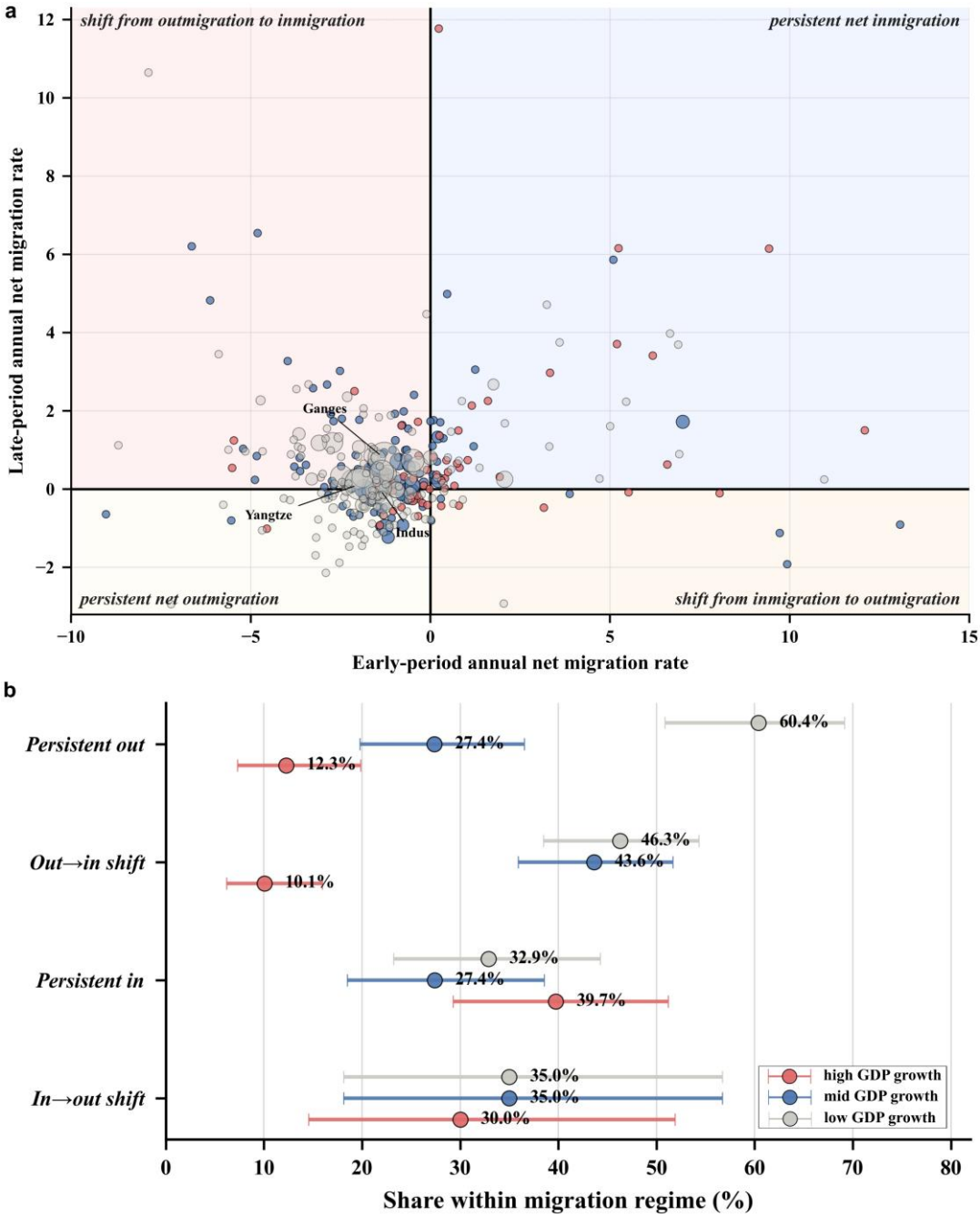
764 indicating stronger flood-exposure pressure relative to economic coping capacity. **d**,

765 Migration regime classification for the Pearl River Basin and neighbouring basins,

766 showing the local spatial context of migration reversal.

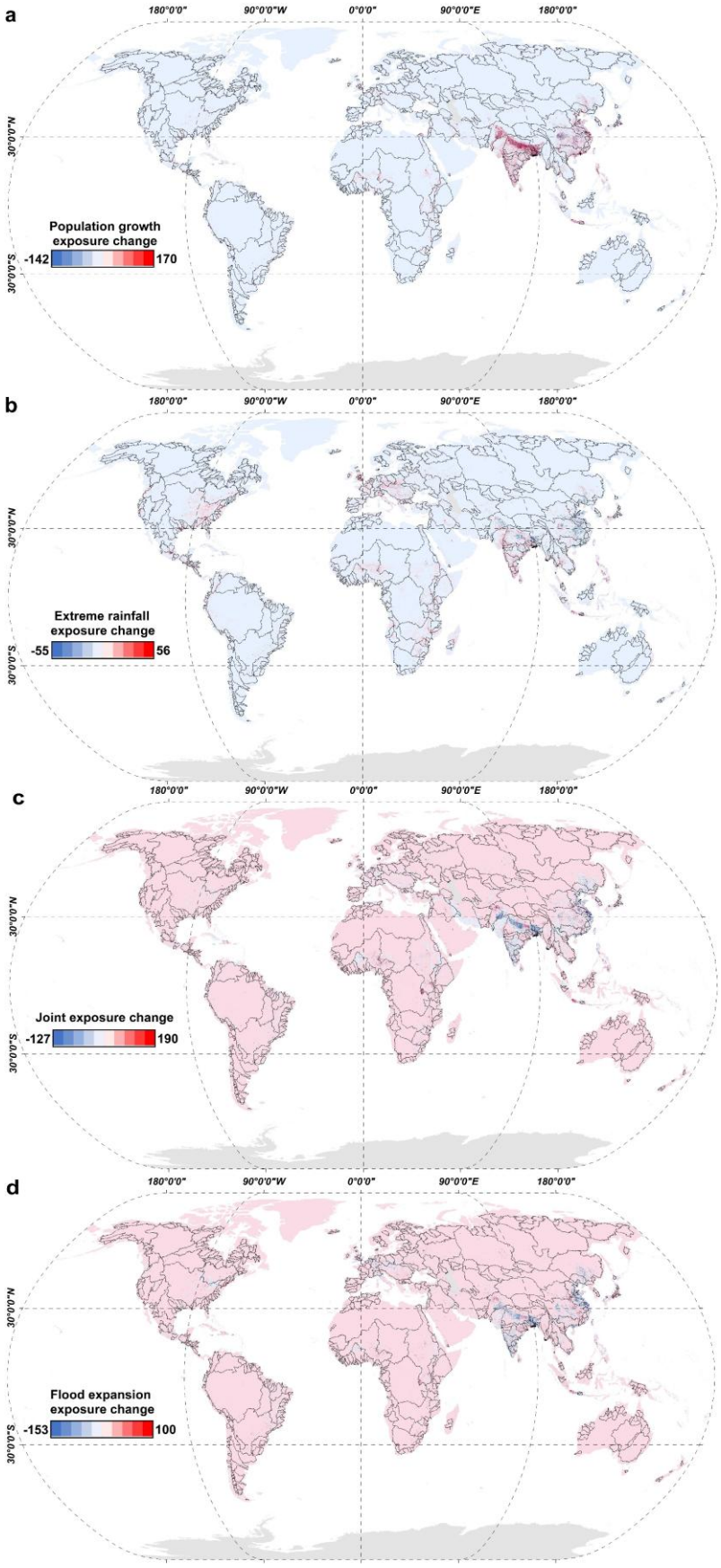


Extended Data Fig. 3 Spatial evidence of migration regime reversal in the Elbe River Basin. a, Flood frequency in and around the Elbe River Basin during 1985-2021. **b**, Pixel-scale exposed-population change. **c**, Basin vulnerability, with higher values indicating stronger flood-exposure pressure relative to economic coping capacity. **d**, Migration regime classification for the Elbe River Basin and neighbouring basins, showing the local spatial context of migration reversal.



Extended Data Fig. 4 Economic growth structure and basin area across migration regimes. a, Quadrant classification of basin migration regimes based on early- and late-period annual net migration rates. Bubble size represents basin area, and colour indicates low-, mid- or high-GDP-growth group. **b**, Shares of GDP-growth groups within each migration regime. Points show percentage shares, and horizontal bars indicate 95% Wilson confidence intervals.

781



Extended Data Fig. 5 Spatial decomposition of exposed-population growth drivers.

a, Exposure change attributed to population growth. **b**, Exposure change attributed to extreme rainfall. **c**, Exposure change attributed to the joint effect of population growth and flood change. **d**, Exposure change attributed to flood expansion. Population growth was the leading contributor to total positive exposure change, accounting for 47.0% of the global positive increase, equivalent to 708.9 million people. Flood expansion contributed 25.5%, or 384.6 million people, followed by the joint term and extreme rainfall. Population-growth-driven change was concentrated in densely populated floodplains of South Asia, eastern China and parts of Southeast Asia and had the strongest local upper tail, with corrected 95th and 99th percentiles of 1.76 and 12.1 persons per pixel, respectively. The joint term had the broadest positive spatial footprint, dominating 48.4% of pixels with at least one positive driver and 46.9% of pixels globally. The flood-expansion term contributed 32.5% of pixels with at least one positive driver and 31.4% of all pixels, whereas extreme rainfall showed the weakest overall contribution and was mainly expressed as localized hotspots.

Supplementary Files

This is a list of supplementary files associated with this preprint. Click to download.

- ExtendedDataFig.2.jpg
- ExtendedDataFig.1.jpg
- ExtendedDataFig.4.jpg
- ExtendedDataFig.5.jpg
- ExtendedDataFig.3.jpg